This is a repository copy of *Characterization of the Structural Environment of Dithionate Ions Associated with Their Role in the Crystal Habit Modification of Sodium Chlorate*.

White Rose Research Online URL for this paper:
http://eprints.whiterose.ac.uk/133237/

Version: Accepted Version

Article:

Lan, Z, Calligaris, GA, de Menezes, AS et al. (4 more authors) (2018) Characterization of the Structural Environment of Dithionate Ions Associated with Their Role in the Crystal Habit Modification of Sodium Chlorate. Crystal Growth & Design, 18 (6). pp. 3328-3338. ISSN 1528-7483

https://doi.org/10.1021/acs.cgd.7b01770

Characterization of the Structural Environment of Dithionate Ions Associated with their Role in the Crystal Habit Modification of Sodium Chlorate

Zhipeng Lan,[1,#] Guilherme A. Calligaris,[2] Alan S. de Menezes,[2,‡]
Adenilson O. dos Santos,[3] Xiaojun Lai,[1,*] Lisandro P. Cardoso[2] and Kevin J. Roberts[1]

[1]Institute of Process Research and Development,
School of Chemical and Process Engineering, University of Leeds, LS2 9JT, UK.
[2]Institute of Physics Gleb Wataghin, University of Campinas – UNICAMP, 13083-859 Campinas, SP, Brazil.
[3]CCSST, Federal University of Maranhão – UFMA, 65900-410 Imperatriz, MA, Brazil.

Key words: Crystal Growth, Habit Modification, EXAFS, X-ray Multiple Diffraction, Sodium Chlorate

ABSTRACT. Sodium chlorate ($NaClO_3$) crystals change from a cuboid to a tetrahedron of $\{\bar{1}\bar{1}\bar{1}\}$ morphology when crystallized in the presence of sodium dithionate ($Na_2S_2O_6$) impurity. Polarized Extended X-Ray Absorption Fine Structure at the S K-edge, used to probe the local structure around this impurity with respect to its orientation within the bulk crystal lattice, reveals that the S-S bond of the $S_2O_6^{2-}$ ions is closely aligned along the <111>/<$\bar{1}\bar{1}\bar{1}$> lattice direction. High resolution diffraction studies using X-ray Multiple Diffraction reveal growth-induced anisotropy in the doped crystals associated with subtle lattice distortions in the symmetry-independent $\{\bar{1}\bar{1}\bar{1}\}$ and {111} growth sectors. The data is consistent with a mechanistic model involving creation of lattice vacancies and the substitution of one of the SO_3 anionic groups of the dopant ion for a host ClO_3 ion when incorporated at the $\{\bar{1}\bar{1}\bar{1}\}$ growth interface with the other

---

[*] Corresponding author email: X.Lai@leeds.ac.uk
Current address of authors
[#] Huadian Coal Industry Group Co. Ltd, 273 Xi Zhi Men Nei Da Jie, Xicheng District, Beijing 100035, China
[‡] Department of Physics, Federal University of Maranhão – UFMA, 65080-805 São Luís, MA, Brazil

SO_3 group substituting for one or more anionic sites in the succeeding growth layer depending on the degree of impurity concentration within the crystallization solution. This mechanism is also fully consistent with the formation of twinning at higher impurity concentrations previously reported by Lan et.al.[7]

1 Introduction

Research into the habit modification of crystals by the presence of impurity ions is not only of practical importance for optimizing crystal morphology resulting from the crystallization process but it also provides useful information regarding the fundamental aspects of the growth process in terms of the inter-relationship between the surface chemistry and interfacial kinetic mechanisms involved in the development of the growth interface. For inorganic systems such heterogeneous additives are presumed to affect the growth rate of individual crystal faces, either by blocking the movement of step/kink sites, or by incorporating into the solid surface and disrupting the inter-ionic bonding networks.[1, 2] Through such processes the shape of a crystal may be changed through the use of habit modifying additives which can only bind to specific crystal faces. Surprisingly, not many habit modifying systems have been studied in any significant detail and thus much knowledge concerning the physical processes associated with the action of such agents still remains completely unknown at this time. Hence, the detailed structural characterization of impurity doped crystals in comparison to this pure crystal reference state can provide a critical assessment of the habit modification process and therefore potentially revealing the mechanism of the impurity incorporation and potential for designing such processes.

The sodium dithionate / sodium chlorate ($Na_2S_2O_6^{2-}$ / $NaClO_3$) impurity / host crystal is a useful representative system for studying crystal habit modification. Sodium chlorate crystallizes in a cubic but enantiomeric crystallographic structure with the space group $P2_13$, four molecules in one unit cell and a lattice parameter a=6.576Å.[3] The crystal habit of pure sodium chlorate at moderate to high supersaturation is cuboid with the {100} form dominating. However, smaller {110} and the major tetrahedral {111} forms tend to appear at lower supersaturations.[4-6] In this structure the <111> is a polar direction and hence the two tetrahedral (polar) forms {111} and $\{\bar{1}\bar{1}\bar{1}\}$ are not structurally equivalent in terms of their respective surface chemistry. The habit modification of $NaClO_3$ in impurity doped growth solutions has been previously examined by Buckley,[4] who explored a total of 36 tetrahedrally and trigonally coordinated anionic impurities. In particular, he observed the dithionate $S_2O_6^{2-}$ ion to be the most effective additive in terms of modifying the habit of $NaClO_3$ in which the normally faster-growing minor tetrahedral $\{\bar{1}\bar{1}\bar{1}\}$ faces are known to appear in the growth morphology and in doing so tend to eliminate the {100} faces. Ristic et al. reported that the impurity-induced tetrahedral faces increased their relative surface area with the $S_2O_6^{2-}$ concentration in the solution, and when it exceeded 210ppm the crystal habit was observed to convert into a pure tetrahedron characterized by the minor tetrahedral $\{\bar{1}\bar{1}\bar{1}\}$ form.[5] Ristic et al also observed that twinning occurred when the dopant concentration exceeded 600ppm.[5, 7]

The previous research has predicted the polar morphology of $NaClO_3$ based on the crystal structure.[8] Previously, the incorporation mechanism of $S_2O_6^{2-}$ in $NaClO_3$ crystal was presumed to involve one of the terminal SO_3 groups of the $S_2O_6^{2-}$ ion substituting for the exposed chlorate ion (ClO_3^-) on the $\{\bar{1}\bar{1}\bar{1}\}$ surfaces. This incorporation mechanism also involved the other terminal SO_3 group being located at an interstitial site with the impurity blocking surface step motion and hence decreasing the velocity of the growing face.[5, 6] However, so far no detailed structural characterization of this habit modification process has been carried out. Recent research, though, has characterized the twinning behavior in sodium chlorate[7] revealing the twin domains to be of the opposite chirality and to be characterized by a merohedral[9, 10] heterochiral interface, i.e. with the lattice of the twin domains being in direct lattice coincidence.

In this study, both the orientation and site symmetry of the dithionate ions within the host crystal lattice are analyzed in order to elucidate the structural mechanism for the impurity incorporation process together with the understanding as to how it mediates the crystal growth. In this, the local structure around the dithionate ion was investigated using polarized Extended X-Ray Absorption Fine Structure (EXAFS)[11] and the impact of its incorporation upon the bulk crystal lattice being assessed with X-Ray Multiple Diffraction (XRMD).[12]

2 Experimental section

2.1 Crystal growth and sample preparation

Sodium chlorate was of ReaventPlus grade (>99%) from Sigma-Aldrich, and the sodium dithionate was in the purity grade >99% from Chemsworth. Both $NaClO_3$ single crystals without and with $S_2O_6^{2-}$ dopant (3.5 x 3.5 x 3.5 cm^3) were grown from the single crystal seeds in water solutions. The solution temperature was decreased 0.5ºC per 12 hours from 45.0℃ to 25.0 ℃. The soluble sodium salt $Na_2S_2O_6$ was added into the growth solutions as a trace impurity at concentrations of 70, 130, 160, 190 and 220ppm, respectively, in order to prepare a range of doped crystals.

A tungsten wire solvent saw was used to cut the crystals into approximate 2 mm plates The surfaces of the plates were polished on moist soft cloths, and then quickly rinsed and gently dried using tissues to remove the residues of fine crystals for the subsequent EXAFS, X-Ray Fluorescence (XRF) and XRMD measurements.

2.2 Experimental characterization

X-ray topographs were received from the diffraction in the transmission mode with a molybdenum X-ray tube as radiation source.

The measurements of Extended X-Ray Absorption Fine Structure (EXAFS) (see S1 in the supplementary material for information of this technique) were conducted at I18 of Diamond Light Source equipped with a Vortex ME-4 fluorescent detector. The crystals were carefully aligned against the beam polarization in order for the information of the impurity orientation within the crystal. To minimize the x-ray absorption by the air, the sample and detectors were all enclosed within a protective environment filled with helium gas. The EXAFS for sulphur K-edge were scanned in the range from 2400 to 2815.85 eV with a step size of 0.25 eV. The computed fitting for EXFAS was carried out by the Demeter system[13] using the crystal structures of $NaClO_3$ and $Na_2S_2O_6$ published in Acta Crystallographica Section B-Structural Science (1977[3] and 1980[14]) respectively. XRF mapping was carried out in an area of a $(\bar{1}10)$ slice from the 190 ppm doped crystal using a single beam energy of 2700 eV to excite the sulphur Kα transition. The beam size of 0.1mm x 0.2mm (VxH) with the scan step of 0.5 mm per second. The beamline software was used to reconstructed the XRF map, e.g. PyMCA package.[15]

X-ray multiple diffraction (XRMD) measurements (see S2 in the supplementary material for information of this technique) were carried out in Renninger scan mode for the large single crystals at XRD1 beamline of LNLS, Brazil.[16] The wavelength was 1.5498(5) Å with the beam size of 1mm x 1 mm. The diffraction peaks on XRMD patterns were indexed by the calculation from the UMWEG program[17] based on the crystal structure of $NaClO_3$ as published by Abrahams and Bernstein (1977).[3]

X-Ray powder diffraction (XRD) data of the impurity doped crystal samples were collected as a reference comparing to the XRMD results. The X-ray diffractometer slit size was 0.5mm and the 2θ detector was scanned from 5º to 80º at a step size of 0.017º. Rietveld refinement method was used to obtained the lattice parameters using HighScore Plus (PANalytical).

The segregation coefficients of the impurity were determined from a comparison between the concentrations of sulphur in the solution and the $NaClO_3$ crystals. The latter was determined through the elemental analysis of incorporated sulphur concentrations using ICP-OES technique at the Butterworth Laboratory[18]. The samples for this measurement were selected from the $(\bar{1}\bar{1}\bar{1})$ growth sectors where the impurity is incorporated during the crystal growth.

Microphotographs of the "as grown" crystal surfaces were taken using an Olympus BX51M optical microscope, equipped with a Carl Zeiss AxioCam MRC5 high-resolution camera.

2.3 Determination of the orientation of the dithionate ions by polarized EXAFS

The EXAFS signal is dependent on the angle between S-S bond and the beam polarization in this case. The relationship is as:

$$\chi_{pol} = 3 \cdot \mathrm{n} \cdot \chi_{iso} \cdot \cos^2 \psi \qquad (1)$$

and

$$\mathrm{N}_{\mathrm{effective}} = \frac{\chi_{pol}}{\chi_{iso}} = 3 \cdot \mathrm{n} \cdot \cos^2 \psi, \qquad (2)$$

where χ_{pol} is the polarized EXAFS, χ_{iso} is the isotropic EXAFS for the powder, ψ provides the angle between the absorber-scatterer vector and the beam polarization vector, and n is the number of equivalent scatters in the distance to the absorber. In this case, both absorber and scatterer are sulphur atom. Therefore the effective coordination number of scattering sulphur ($\mathrm{N}_{\mathrm{effective}}$) is calculated as $3\mathrm{n} \cdot \cos^2 \psi$. Using this relationship, the sample orientation and the beam polarization, the impurity orientation within the crystal was determined.

2.4 Structure factor calculations

For the evaluation of the effect of the $S_2O_6^{2-}$ incorporated in the $NaClO_3$ crystal lattice, notably the disturbances caused to the crystal chemistry, the structure factors for the associated secondary XRMD reflections of interest were calculated. In this, the effect of the impurity on the crystal lattice was simulated using a temperature factor in the calculation specifically for the sites of the O atom in the $NaClO_3$ crystal (Equation 3).

$$F = f_{Na}\left(\sum_{n=1}^{4} e^{2\pi i(hx_n+ky_n+lz_n)}\right)_{Na} + f_{Cl}\left(\sum_{n=1}^{4} e^{2\pi i(hx_n+ky_n+lz_n)}\right)_{Cl} + f_O\left(\sum_{n=1}^{4} e^{2\pi i(hx_n+ky_n+lz_n)}\right)_{O} e^{-8\pi^2\langle u^2\rangle\left(\sin\frac{\theta}{\lambda}\right)^2} \quad (3)$$

where f_{Na}, f_{Cl} and f_O are the atomic scattering factors for Na, Cl and O atoms, i is the imaginary number, $\langle u^2\rangle$ is the mean-squared displacement of the O atoms owing to the presence of $S_2O_6^{2-}$ ions in the crystal lattice, θ and λ denote the Bragg angle and wavelength of the incident beam.[25]

The rationale for this reflects the fact that these sites would be the most likely sites to be disrupted by the effects of the impurity incorporation mindful of the larger size of the dithionate ion with respect to the smaller host chlorate ion (see section 3.4). Modified structure factors were normalized to those calculated without the temperature factor, i.e. for the case of pure crystal.

2.5 Crystalline quality evaluation

To assess the crystal quality in the presence of the impurity, the mosaic spread both in-plane ($\eta_{\text{in-plane}}$) and perpendicular (η_{perp}) with respect to the diffraction planes, respectively, were calculated using:

$$\eta_{perp} = \frac{FWHM_{perp}}{2.355} \tag{4}$$

and

$$\eta_{in-plane} = \frac{FWHM_{in-plane}}{2.355} \quad , \tag{5}$$

where $FWHM_{perp}$ and $FWHM_{in\text{-}plane}$ were received using Gaussian fit for ω:ϕ maps of BSD cases along the ω and ϕ directions, respectively.[19]

3 Results and discussion

The experimental data is presented in 3 sections in which distinct contributions from each technique are discussed in detail, and leads to a final section with the proposed incorporation model for sodium dithionate. Firstly, in 3.1, the habits from pure and doped samples are discussed and then related to XRF mappings. Then, section 3.2 the EXAFS characterizations of the dithionate ion orientation as incorporated into the $NaClO_3$ lattice. Then, section 3.3 presents the XRMD results and evaluates the impact of the $S_2O_6^{2-}$ ion incorporation into the $NaClO_3$ lattice in terms of the lattice strains crystalline quality and growth-induced anisotropy. Finally, section 3.4, the structural similarities between ClO_3^- and $S_2O_6^{2-}$ ions are examined and EXAFS, XRMD and surface morphology microscopy data is integrated through the development of a self-consistent incorporation model.

Although the crystal samples for this study can have either the left handedness or the right handedness, the dithionate ion substitution processes and the characterization techniques applied are not sensitive to the chiral structure of sodium chlorate. Thus, this article keeps the convention used in the previous publications[7] that $\{\bar{1}\,\bar{1}\,\bar{1}\}$ is the direction pointed by the Chlorine of a chlorate ion, in order to avoid the possible inconsistency for defining the impurity modified face type.

3.1 Crystal growth, associated habits and growth sector selectivity incorporation

For the solution cooling rates used in this work, the pure as-grown crystals morphology comprised the $\{100\}$ and $\{110\}$ forms. In the presence of $S_2O_6^{2-}$ impurity in the growth solution, the tetrahedral $\{\bar{1}\,\bar{1}\,\bar{1}\}$ form was found to develop and to dominate the morphology even at the lowest 70 ppm impurity level (Figure 1) examined. Table 1 gives the main details related to the two tetrahedral forms for $NaClO_3$.

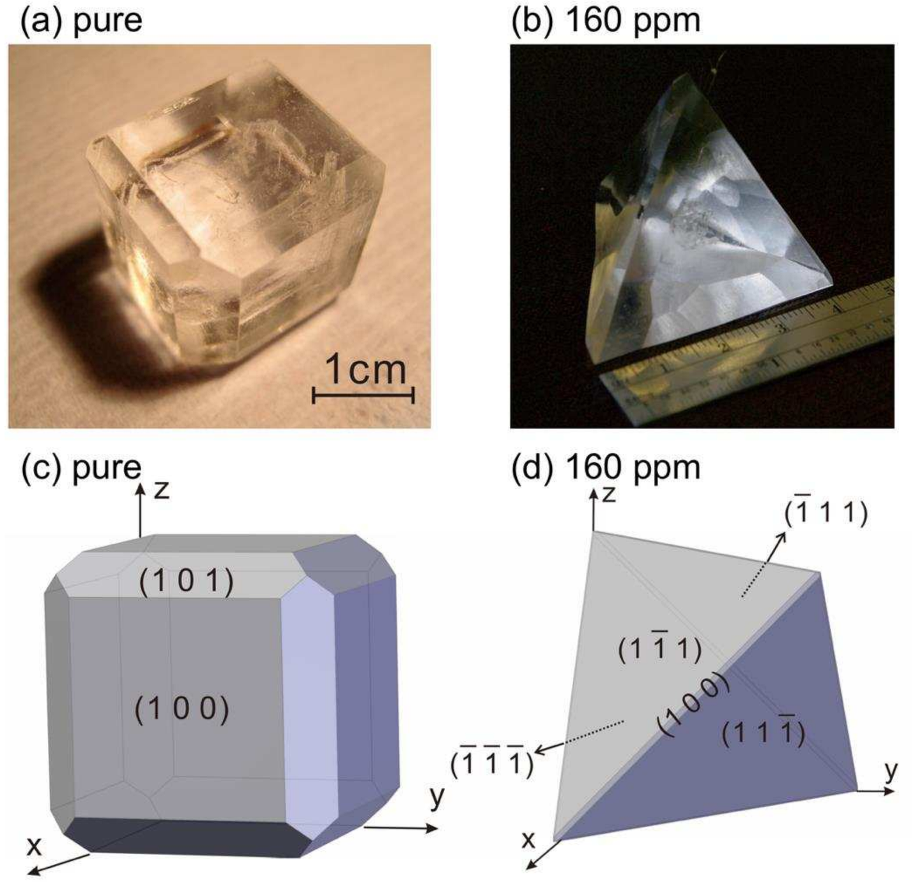

Figure 1. Shows the crystal morphologies of $NaClO_3$ as a function of solution concentration of impurity. **(a)** Pure $NaClO_3$ crystal; **(b)** $NaClO_3$ crystal grown from 160 ppm $S_2O_6^{2-}$ solution concentration; **(c)** Drawing of morphology of the pure crystal; **(d)** Drawing of the morphology of the doped crystal from 160 ppm $S_2O_6^{2-}$ concentration solution.

Table 1. The two independent tetrahedral forms for $NaClO_3$, which are inherent for this material enantiomeric space group $P2_13$.

Form type	Form	Constituent Faces	Crystal Morphology
Major tetrahedral	$\{111\}$	(111), $(\bar{1}\bar{1}1)$, $(\bar{1}1\bar{1})$, $(1\bar{1}\bar{1})$	Small faces in pure crystals only appearing for the lower cooling rates
Minor tetrahedral	$\{\bar{1}\bar{1}\bar{1}\}$	$(1\bar{1}1)$, $(\bar{1}11)$, $(\bar{1}\bar{1}\bar{1})$, $(11\bar{1})$	Form only appears upon the addition of habit modifying impurities such as $Na_2S_2O_6$

XRF-mapping using S Kα photons was performed to characterize the distribution of $S_2O_6^{2-}$ ions as incorporated within the growth sectors of a doped crystal. Figure 2 (b) shows the sulphur distribution in a selected area of a 190ppm impurity doped $(\bar{1}10)$ crystal plate. The x-ray topographic image in Figure 2 (a) clearly illustrated the growth sectors. It assists to identify the sulphur distribution (Figure 2(b)) in the growth different sectors. The mean values of photon counting of sulphur Kα fluorescence for {001} and $\{\bar{1}\bar{1}\bar{1}\}$ growth sector types were found to be 4981 and 10890 counts per second, respectively.

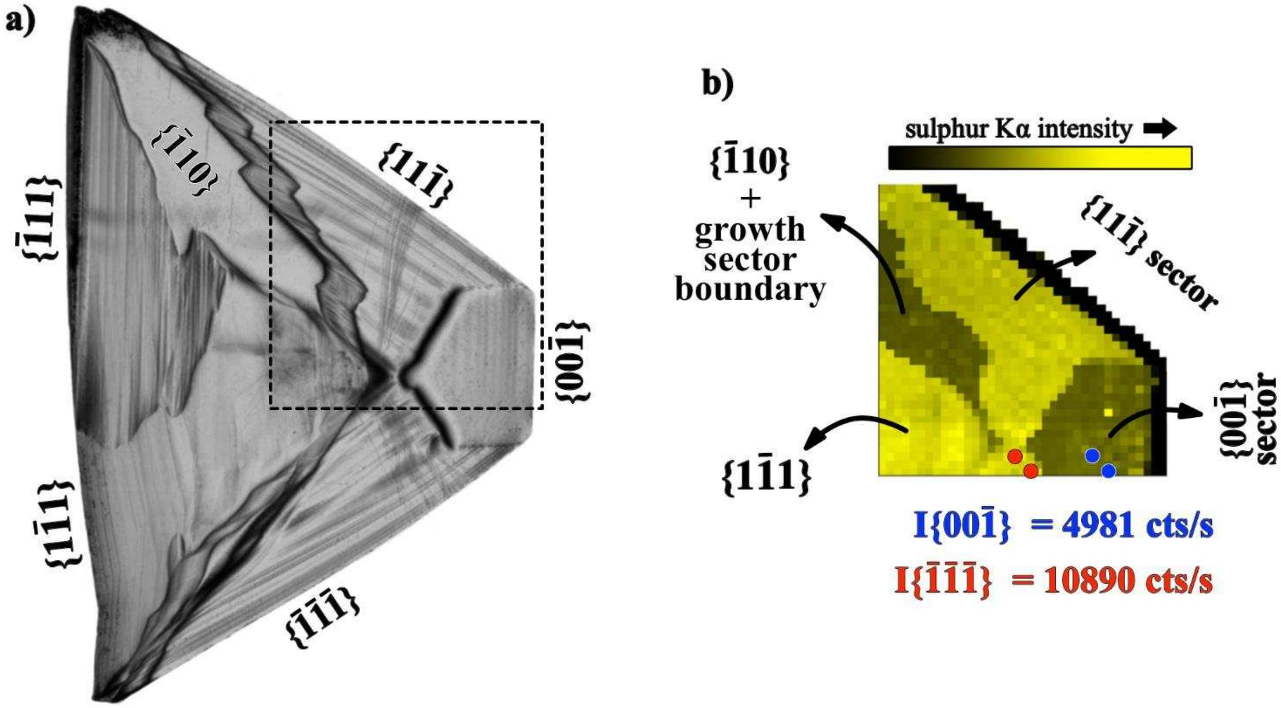

Figure 2. (a) X-ray topograph of the $(\bar{1}10)$ plate from 190 ppm crystal as characterized using XRF-mapping. The growth sectors involved are indexed. **(b)** Sulphur Kα XRF-map of the selected region highlighted in (a). Intensity count was carried out on the pixelated areas shown and in two different growth sectors. A single spot of higher concentration of sulphur (seen as bright yellow) in the $\{00\bar{1}\}$ is inconsistent with the rest area of the sector. This might be due to the beam scattering.

XRF mapping showed that the sulphur has a significantly higher concentration in the $\{\bar{1}\bar{1}\bar{1}\}$ than that in the $\{00\bar{1}\}$. This indicates that $S_2O_6^{2-}$ was incorporated not only in the $\{\bar{1}\bar{1}\bar{1}\}$ sector, but also, at lower concentrations, in the $\{00\bar{1}\}$.

3.2 Orientation of the incorporated dithionate ions

EXAFS measurements were made for the $(\bar{1}10)$ plate cut from the crystal from the 190 ppm impurity concentration solution. Data was collected with two crystal orientations where the crystal $[\bar{1}\ \bar{1}\ \bar{1}]$ axis was either parallel (orientation I) or perpendicular (orientation II) beam polarization direction. This approach was used to characterize the impurity orientation once incorporated in the lattice reflecting upon the proposed $S_2O_6^{2-}$ incorporation model by Ristic et al[5, 6]. Figure 3 shows the fitted spectra of EXAFS for the orientations I and II, while Table 2 and 3 provide the parameters received from the EXAFS fittings, in particular for the sulphur coordination numbers ($N_{effective}$) in the 2nd shell. Because of the low concentration of the impurity in the crystal sample, the EXAFS signal was too noisy when the energy is 260 eV above the sulphur K-edge, so that the data cannot reliably fitted for the oxygens in 3rd shell.

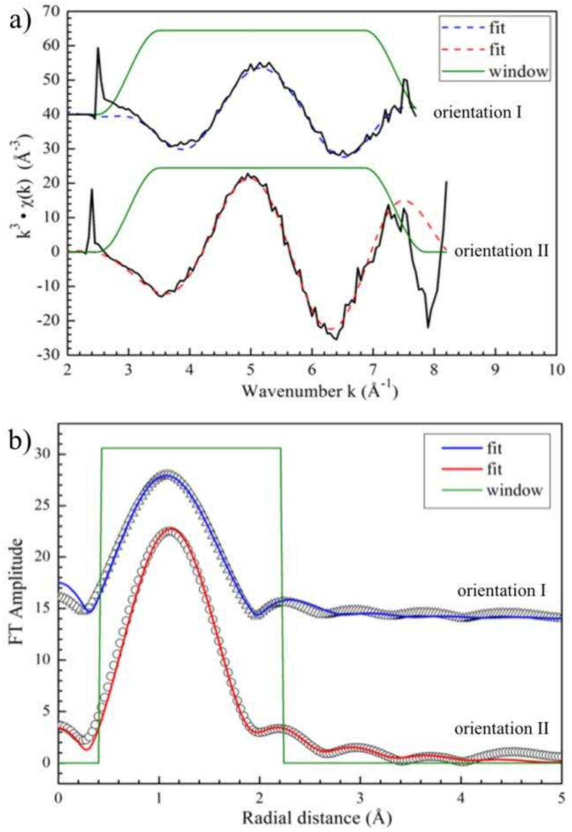

Figure 3. (a) The $k^3\chi$ curves of the 190ppm sample and the best-fits for beam polarization parallel (orientation I) or perpendicular (orientation II) to the $[\bar{1}\ \bar{1}\ \bar{1}]$ axis. **(b)** The best-fits for the Fourier transforms of the $k^3\chi$ for the limited radial distance range shown as the green. Because the phase-shift correction process was carried out for Fourier transform, the appeared peak positions in the plot are slightly shifted from the actual values of the bond lengths determined.

Table 2. EXAFS fitting results for $S_2O_6^{2-}$ ion in crystal at the crystal orientation that beam polarization vector is parallel to the $[\bar{1}1\bar{1}]$ direction (i.e. orientation I). S1 indicates the absorbing sulphur atom, whereas S2 indicates the scatterer atom of sulphur as in the 2nd shell. The effective coordination number $N_{effective}$ is the total number of the atoms in the shell. $R_{theo.}$ and $R_{exp.}$ are the theoretical and the evaluated experimental radial distances, respectively, and for the second shell this distance should be approximately equal to the bond length S-S in $S_2O_6^{2-}$ ion. ΔR is the difference between the theoretical and experimental values. σ^2 is the mean-square disorder of neighbor distance due to thermal vibration.

Shell no.	Shell atom	Scattering path	$N_{effective}$	$R_{theo.}$	ΔR (Å)	$R_{exp.}$ (Å)	σ^2 (Å^2)
1	Oxygen	S1→O→S1	3.7	1.4512	-0.0209(±0.003)	1.4303	0.0003
2	S2	S1→S2→S2	2.9	2.1399	0.0920(±0.005)	2.2296	0.0025

Table 3. EXAFS fitting results for $S_2O_6^{2-}$ ion in crystal at the crystal orientation that the beam polarization vector is perpendicular to the $[\bar{1}1\bar{1}]$ direction (i.e. orientation II). Atom nominations and symbols are the same as in Table 2.

Shell no.	Shell atom	Scattering path	$N_{effective}$	$R_{theo.}$	ΔR (Å)	$R_{exp.}$ (Å)	σ^2 (Å^2)
1	Oxygen	S1→O1→S1	6.7	1.4512	-0.0229(±0.003)	1.4283	0.004
2	S2	S1→S2→S1	0	N/A	N/A	N/A	N/A

In Table 2 and 3, the two sample orientations provide very different coordination numbers of Sulphur. When the beam polarization vector is parallel to the $[\bar{1}1\bar{1}]$ direction, the sulphur $N_{effective}$ of 2.9 indicates that the S-S bond has a portion of alignment along the $[\bar{1}1\bar{1}]$ direction. In contrast, when the beam polarization vector is perpendicular to the $[\bar{1}1\bar{1}]$ direction, the sulphur $N_{effective}$ is zero, which means S-S bond is perpendicular to the beam polarization vector or the $[\bar{1}1\bar{1}]$ direction. Relating $N_{effective}$ and equation 2 for orientation I gives a ψ of ~0°, i.e., the S-S bond is aligned with the x-ray beam polarization (S-S//$\vec{e}$). On the other hand, a ψ of ~90° for orientation II means that S-S has no projection on the polarization plane (S-S$\perp\vec{e}$). Consequently, this result reports that the S-S is dominantly aligned in the $[\bar{1}1\bar{1}]$ direction (i.e. perpendicular to the $(\bar{1}1\bar{1})$ surface).

3.3 Impact of impurity incorporation on the bulk crystal lattice

3.3.1 Lattice disturbance after dithionate incorporation

In order to examine the lattice distortion caused by the incorporation of $S_2O_6^{2-}$ ions in the $NaClO_3$ crystal, Renninger Scans[19] (RS) using the (004) as primary reflection were performed for all the pure and doped crystals. Figure 4(a) shows the RSs of a pure crystal around ϕ=0º mirror. Comparing the number and the positions of XRMD peaks of the pure and doped crystals, all the RS profiles were found to be very similar which indicates no significant change in the overall crystal symmetry through the incorporation of the dopant dithionate ions. Despite this, a closer examination of the peak profiles revealed some subtle peak intensity changes for the crystals of different impurity doping concentrations. Figure 4(b) shows details of the RS reflections in 1.4º range at both sides of the symmetry mirror ϕ = 0º. For the pure crystal, the secondary peaks $(3\bar{4}3)(3\bar{4}1)$, $(343)(341)$, $(1\bar{3}3)(1\bar{3}1)$ and $(133)(131)$ are of the four-beam case, which involves the incident beam, the primary reflection beam together with two simultaneous secondary diffracted beams. However, for the doped samples, two sets of secondary peaks, i.e. $(3\bar{4}3)(3\bar{4}1)$ and $(343)(341)$, were found to have almost disappeared or, at most, their peak profiles became asymmetric with significantly reduced intensity. In contrast, the $(1\bar{3}3)(1\bar{3}1)$ and $(133)(131)$ peaks remained unchanged. This result clearly implies that the presence of the $S_2O_6^{2-}$ impurity has affected the crystallographic packing close to these atomic planes associated with the impurity incorporation at the specific faces.

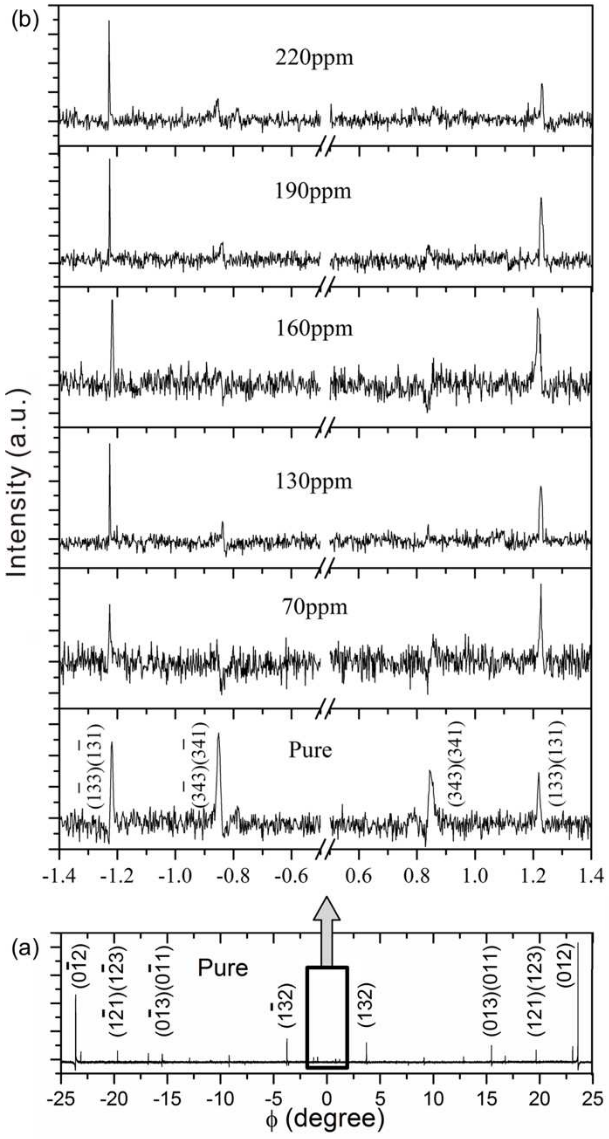

Figure 4. (a) Broad view of (004) Renninger Scan around ϕ=0° for pure samples. **(b)** Expanded view of the RS around ϕ=0° for all the examined samples. The four specific peaks related with different four-beam cases are indexed in the figures, of which the intensities of $(3\bar{4}3)(3\bar{4}1)$ and $(343)(341)$ were significantly reduced for the doped crystals.

The phenomenon of intensity reduction to the secondary peaks has often been observed for impurity doped crystal systems, for example, Ni-doped L-histidine hydrochloride monohydrate[20] and Mn-doped potassium dihydrogen phosphate,[21] where the impurity incorporation slightly disturbs the nearby ion groups in the crystal lattice and hence sensitively changes the structure factors associated with some secondary diffractions.

For this, the structure factors of the diffraction from the $(3\bar{4}3)(3\bar{4}1)$ and $(343)(341)$ planes were calculated by considering changes on the displacement of O atoms, which are most likely disturbed upon the incorporation of $S_2O_6^{2-}$. Figure 5 demonstrates the changes to the structure factors of (343)(341) and (133)(131) planes when a small displacement (u) takes place to the O atoms of the ClO_3^{2-}, as calculated in Equation 3. These calculations reveal that the structure factor of the (343) plane has a much higher sensitivity to the oxygen atom displacement comparing to the other three planes, as evidenced through the fact that its structure factor rapidly decreases with the increase of the degree of the oxygen atom displacement. As a result, it can be expected that the diffraction intensity of the (343)(341) four-beam case peak would decrease significantly, whilst the effect for the (133)(131) would be expected to be much less. Thus, the peak suppression for the $(3\bar{4}3)(3\bar{4}1)$ and (343)(341) suggests a position displacement for the O atoms or for the ClO_3^{2-} ion when the $S_2O_6^{2-}$ is incorporated at the $\{\bar{1}\bar{1}\bar{1}\}$ surfaces of the $NaClO_3$ crystal.

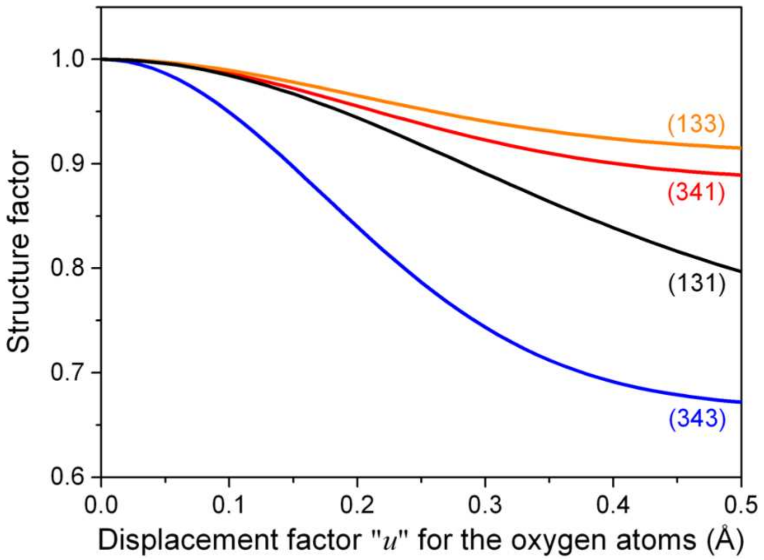

Figure 5. The variation of normalized structure factors for different diffraction planes evaluated when a small displacement takes place to the oxygen atom as a result of being disturbed by the impurity incorporation. The structure factor of each plane was normalized against that calculated for the pure crystal. The structure factor for the (343) plane can be seen to decrease as a function of O atom displacement much more than for the cases of the other three planes.

3.3.2 Distinct strains observed in $\{\bar{1}\bar{1}\bar{1}\}$ and $\{111\}$ forms

The XRF data, discussed earlier in 3.1, reveals that the $S_2O_6^{2-}$ impurity is preferentially incorporated within the $\{\bar{1}\bar{1}\bar{1}\}$ growth sectors (Figure 6 (a) and (b)) over the $\{111\}$ form (Figure 6 (c) and (d)). Using the (002) primary diffraction, the above two sets of secondary planes can be measured as Bragg-Surface Diffraction[22] (BSD) three-beam cases through RS made around the ϕ = 45º mirror, (002)(111) and (002)($\bar{1}\bar{1}1$), and the ϕ = 135º mirror, (002)($1\bar{1}1$) and (002)($\bar{1}11$). This information is summed in Table 4 and is shown in Figure 7 (a) and (b), respectively.

Table 4. The two assessments of XRMD measurement for each of the tetrahedral forms.

Form type	Form	Constituent Faces	XRMD Assessment
Major tetrahedral	$\{111\}$	(111), $(\bar{1}\bar{1}1)$	(002) RS ϕ = 45º mirror
		$(\bar{1}1\bar{1})$, $(1\bar{1}\bar{1})$	-
Minor tetrahedral	$\{\bar{1}\bar{1}\bar{1}\}$	$(1\bar{1}1)$, $(\bar{1}11)$	(002) RS ϕ = 135º mirror
		$(\bar{1}\bar{1}\bar{1})$, $(11\bar{1})$	-

Figures 6 (a) and (c) show the beam paths for the above diffraction cases. It illustrates that the $(1\bar{1}1)$ and $(\bar{1}11)$ secondary diffracted beams respectively travel in the directions of $[1\bar{1}0]$ and $[\bar{1}10]$ parallel to the primary diffraction planes, and that the (111) and $(\bar{1}\bar{1}1)$ secondary diffracted beams respectively travel in the direction of $[110]$ and $[\bar{1}\bar{1}0]$ parallel to the primary diffraction planes. Thus, the beam paths associated with the two different pairs of diffraction peaks 90º each other around the ϕ-axis (perpendicular to the sample surface) and correspond to the two growth fronts in the crystal. This diffraction geometry enables an easy selection between which tetrahedral form planes diffract and hence this set-up can be used to select which tetrahedral form is to be examined.

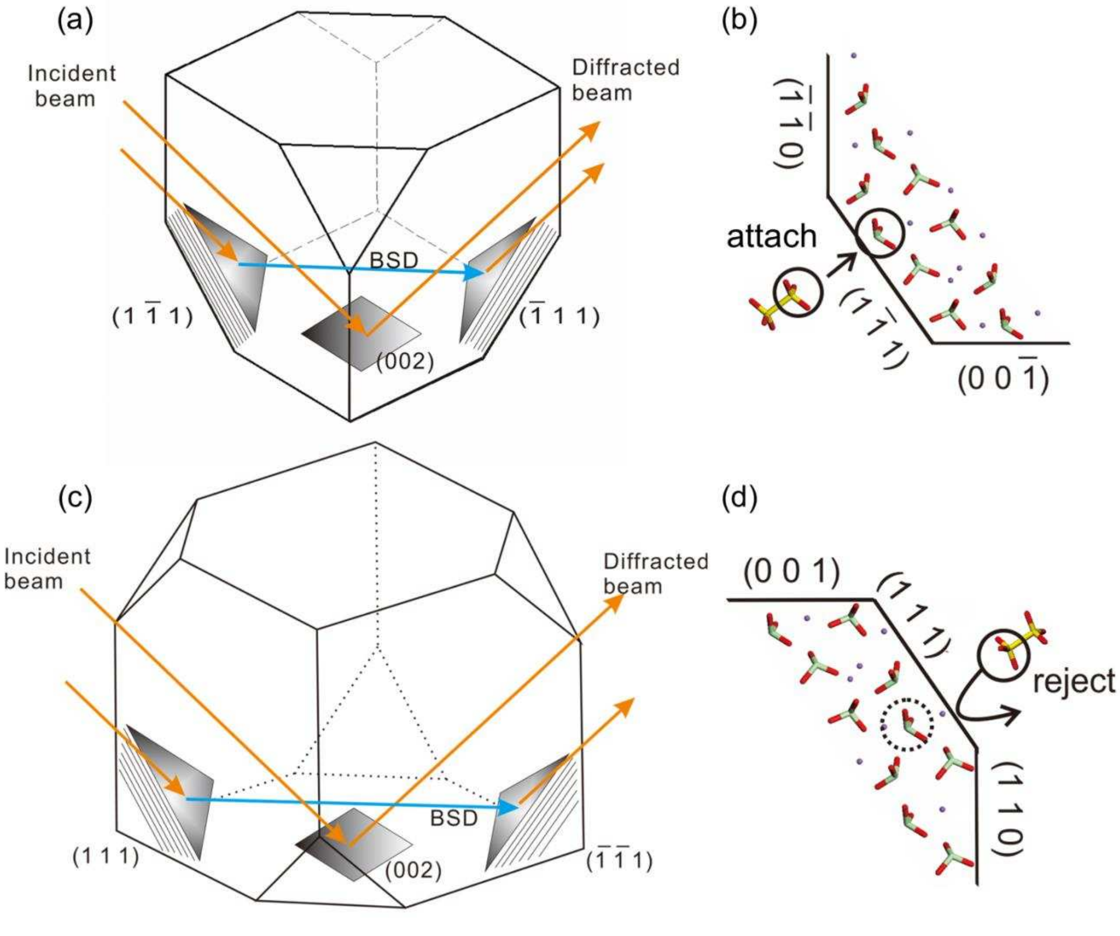

Figure 6. Sketch of the selection of different BSD beam paths under (002) primary diffraction for probing the crystal surfaces of impurity incorporation. **(a)** The beam path for BSD case: $(1\bar{1}1)$ secondary and $(\bar{1}11)$ coupling planes (minor tetrahedral). **(b)** The surface chemistry of the $(1\bar{1}1)$ face, which facilitates the incorporation of the impurity. **(c)** The beam path for the BSD case: (111) secondary and $(\bar{1}\bar{1}1)$ coupling planes (major tetrahedral). **(d)** The surface chemistry of the (111) face, which results in the rejection to the impurity. Note: The two beam paths shown in (a) and (c) are rotated by 90° around the ϕ-axis.

Examination of the distance between the secondary peaks shown in Figure 7(a) reveals that the peak separation is increased with the impurity concentration, whilst those in Figure 7(b) show the opposite trend, i.e. contracting towards each other with increasing impurity concentration. However, in the unstrained cubic lattice of an ideally perfect crystal, the trend of this change should be identical, i.e. the peak separation between the (111) and $(\bar{1}\bar{1}1)$ at both sides of the ϕ = 45º symmetry mirror should be same as that between the $(1\bar{1}1)$ and $(\bar{1}11)$ around the ϕ = 135º symmetry mirror. Thus, the distinctive behavior of the peak separation with increasing impurity shown in Figure 7(a) and (b) implies the presence of growth-induced structural anisotropy consistent with a trigonal lattice distribution with opposite sense along the two different directions of the <111> polar axis.

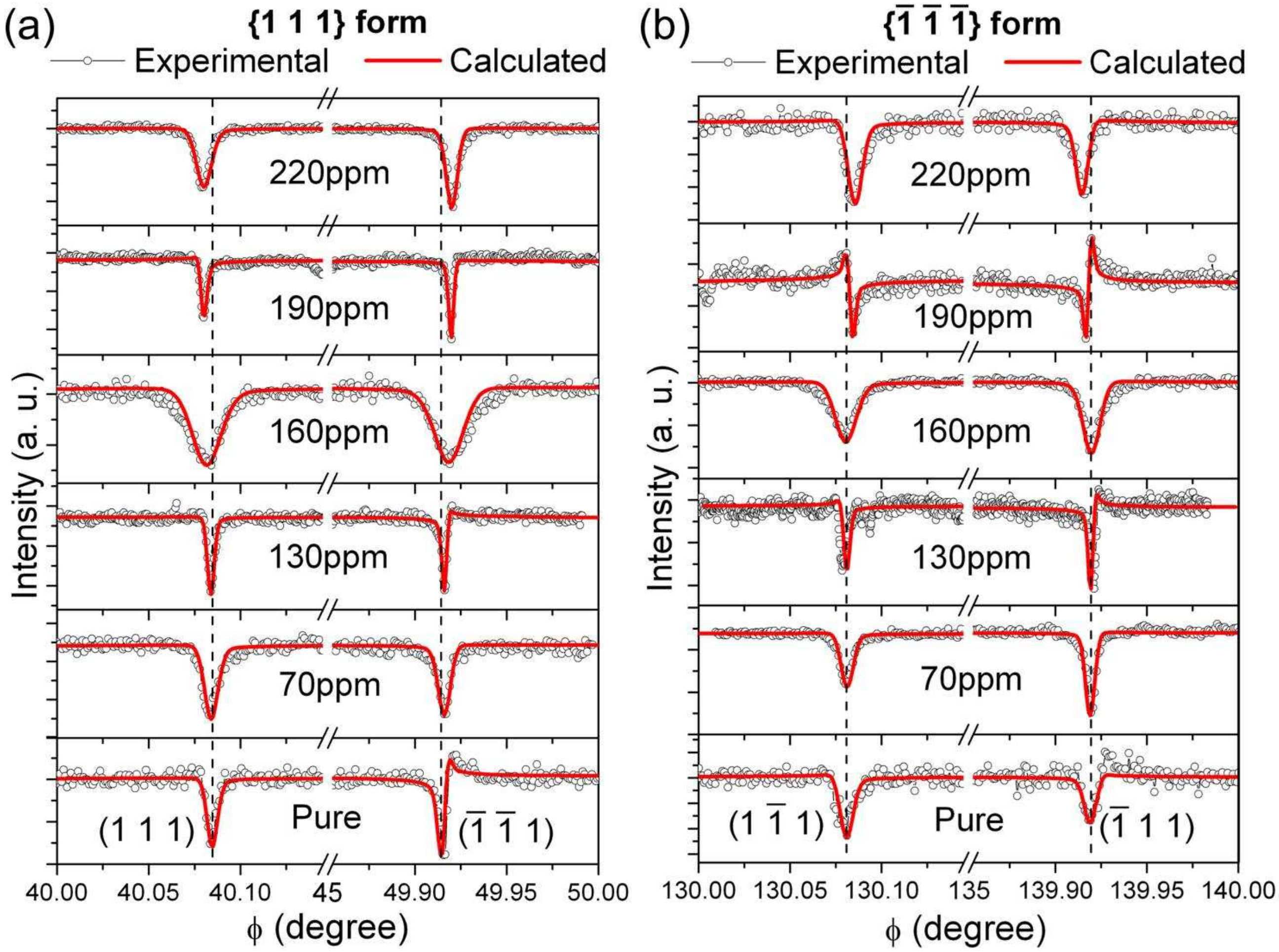

Figure 7. Effect of impurity in (002) RS by calculation fitting of the BSD cases. **(a)** Major tetrahedral form involving (111), $(\bar{1}\bar{1}1)$ planes showing that their diffracted peak separation increases with the impurity concentration; **(b)** Minor tetrahedral form involving $(1\bar{1}1)$, $(\bar{1}11)$ planes showing that their diffracted peak separation has an opposite trend to the case of (a).

The lattice parameters for the single crystal samples as measured as a function of impurity content are given in Figure 8(a). These are based on the results of XRMD for the (002) RSs and XRD. The Rietveld analysis for the XRD data did not indicate any change of the lattice parameters as a result of the impurity incorporation. However, the XRMD results, due to their ability to assess differences between the non-equivalent [111] and $[\bar{1}\bar{1}\bar{1}]$ growth directions, revealed subtle but significant differences. Specifically, the analysis reveals different lattice parameters when calculated from the positions of the (111) and $(\bar{1}\bar{1}1)$ secondary XRMD peaks which probe growth on the major tetrahedral {111} forms when compared to the same for the $(1\bar{1}1)$ and $(\bar{1}11)$ secondary XRMD peaks which probe growth on the minor tetrahedral form $\{\bar{1}\bar{1}\bar{1}\}$. Such an observation is consistent with growth rate anisotropy associated with a slight trigonal distortion of $\Delta d/d \approx 4.6 \times 10^{-4}$ along the <111> direction with a dilation of the lattice for the major tetrahedral form {111} coupled with a compression of the lattice for the minor form.

It is very interesting to observe that the lattice parameters in the {111} and $\{\bar{1}\bar{1}\bar{1}\}$ regions display the opposite variations with respect to the increased impurity concentration, i.e. the major tetrahedral {111} lattice parameter decreases with the increase of impurity concentration whilst the minor tetrahedral form $\{\bar{1}\bar{1}\bar{1}\}$ lattice parameter increases over the same range. An analogous behavior has been observed previously for $NaClO_3$ doped with c.a. 50ppm $Na_2S_2O_6$,[6] where the optical interferogram for the growth observation showed that the $\{\bar{1}\bar{1}\bar{1}\}$ faces has a curved morphology with the two unequal main radii along the a and b directions of the crystal.

Since the lattice parameter of the $\{\bar{1}\ \bar{1}\ \bar{1}\}$ form for the doped crystals was calculated from the $(1\bar{1}1)$ and $(\bar{1}11)$ secondary diffractions and was found to be increased comparing with that of the pure crystals (e.g. in Figure 8(a)), it can be rationalized that a tensile strain induced by the incorporated impurity at the $(1\bar{1}1)$ and $(\bar{1}11)$ planes would dilate the crystal lattices and hence increased the lattice parameter. It was found that the higher the impurity concentration, the higher the tensile strain. At the same time, the (111) and $(\bar{1}\bar{1}1)$ planes were found to be compressed. This maintains the lattice volume unchanged. Therefore, the increase in compressive lattice strain is responsible for the decrease in the lattice parameter (e.g. see Figure 8(a)) received from (111) and $(\bar{1}\bar{1}1)$ planes in RS.

There is an interesting anomaly in both lattice parameters (Figure 8(a)) and strain (Figure 8(b)) data for the 160ppm dopant level. The reason for this is not completely clear at this time but might reflect the formation of a highly defective surface layer at this dopant level. Clearly, more measurements at more closely-spaced impurity intervals are needed to resolve whether this feature is real or simply an artefact of this specific series of measurements. The observation that the lattice parameter obtained from the powder diffraction data do not change as a function of impurity is not unexpected, i.e. they simply reflect the average value based on reflection on all the {111} planes further averaged over a number of microcrystals. Additionally, the grinding of the crystals needed to make a powder is likely to relax any strain present within the powdered crystal samples.

According to previous studies, the application of an externally-induced strain can decrease the growth rate of a given crystal surface in two ways.[23, 24] Such a strain can increase the free energy of the surface, which in turn, results in the obstruction in the motion of growth steps. On the other hand, the strain can raise the surface chemical potential, resulting in a decrease of the driving force for crystal growth. Based on this rationale it can be concluded that the strain induced by the incorporation of $S_2O_6^{2-}$ at the $\{\bar{1}\bar{1}\bar{1}\}$ surfaces has retarded the growth rate of these faces. This has, in turn, effected the habit modification of the $NaClO_3$ crystals from a cuboid morphology to a morphology dominated by the minor tetrahedra.

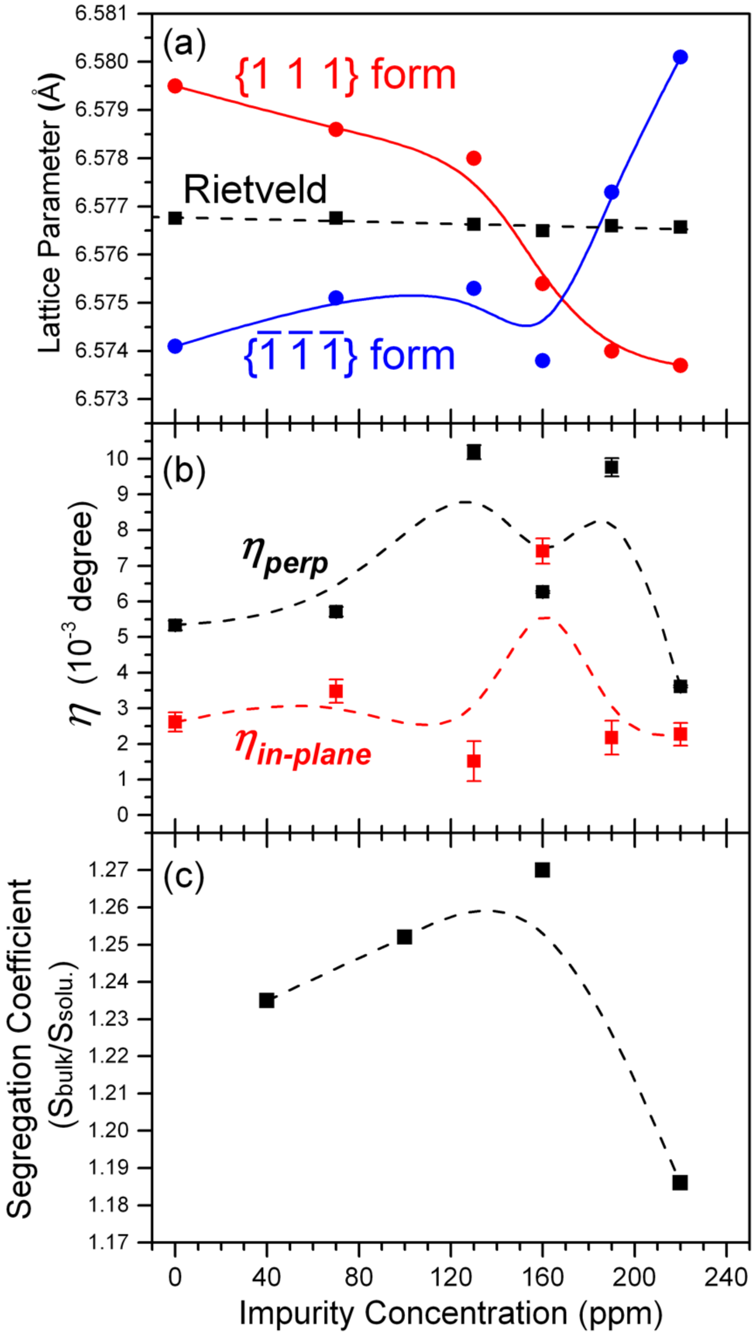

Figure 8. (a) The effect of the impurity concentration on the lattice parameters characterized by XRMD RS and XRD Rietveld analysis. The results obtained from the {111} and $\{\bar{1}\bar{1}\bar{1}\}$ forms indicate opposite variation tendency lying on the high sensitivity of XRMD, while the Rietveld analysis values did not significantly change; **(b)** Evaluated Mosaic spread values in the perpendicular (η_{perp}) and parallel ($\eta_{\mathrm{in\text{-}plane}}$) directions of to primary diffraction planes; **(c)** Segregation coefficient as a function of the impurity concentrations in the crystal growing solution. The dotted line only shows the trend of segregation coefficient variation.

3.3.3 Crystalline quality by ω:ϕ mappings

The ω:ϕ mappings around peaks were used to complement the BSD XRMD data in particular to characterize the lattice strain and its spatial distribution within the sample surfaces. However, directly mapping the reflection of $\{111\}$ or $\{\bar{1}\bar{1}\bar{1}\}$ types was not feasible, reflecting the fact that they are Aufhellung (negative) peaks of weak intensity. In other words, part of the strong primary reflection is diffracted as the BSD secondary reflection which is then redirected by the reflection of the coupling planes back into detected X-ray intensity. These BSD beams appear as the dips in the (002) RS (as shown in Figure 7). Hence, in order to investigate the strain at the crystal surface, the alternative, much stronger, (004) RS with (012) as the secondary and BSD reflection was chosen for ω:ϕ mapping, due to the BSD condition (hkl)=$(hk2)$.[12] Figure 9 shows the (012) ω:ϕ X-ray scattering maps for both pure and doped crystal diffraction peaks, the latter as a function of impurity concentration (70, 130, 160, 190 and 220ppm). The peak widths along the perpendicular (ω) and in-plane (ϕ) lattice directions provide a strong indication as to the crystal quality, i.e. the narrower the peak widths in both ϕ and ω directions, the higher the crystal perfection. As can be seen, the pure, the 70ppm and the 220ppm impurity doped crystals have relatively small ω and ϕ widths. These widths for 130 and 190 ppm doped crystals are intermediate. However, it is noteworthy that the 160ppm doped crystal have a significantly wider peak in the ϕ direction.

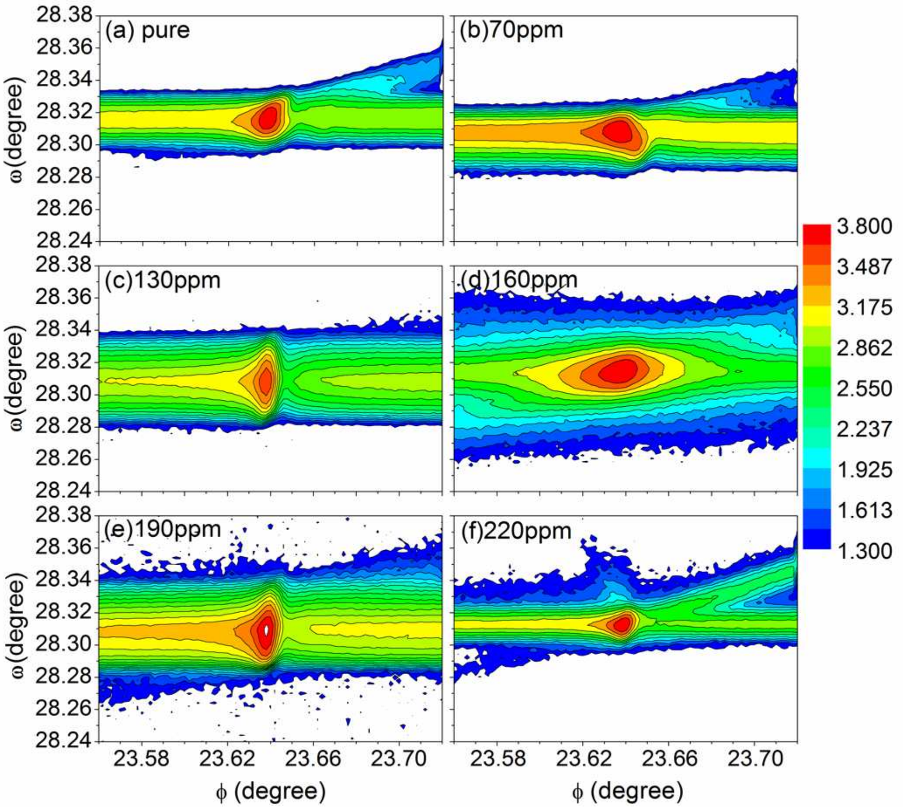

Figure 9. Crystal perfection mapping using ω:ϕ scan around the BSD secondary diffraction of (012) with the (004) as the primary reflection for the pure crystal and the crystals with different impurity doping concentrations. The 160ppm doped crystal exhibits a higher strain along in-plane directions, since its peak in ϕ is much wider in comparison to the other samples.

The calculated η_{perp} and $\eta_{\text{in-plane}}$ strain values obtained from the analysis of the (012) BSD ω:ϕ mapping data in Figure 9 are shown in the Figure 8(b). By comparing the data for the pure crystal, it was found that in some samples both the η_{perp} and $\eta_{\text{in-plane}}$ are increasing or decreasing together as a function of impurity doping concentration, e.g. the 70ppm and 160ppm doped crystals have the case of increasing, whereas the two Mosaic spread values decreases with the increased doping concentration for the 220ppm sample. In contrast, the η_{perp} increases while the $\eta_{\text{in-plane}}$ decreases in the 130ppm and 190ppm doped samples. It is interesting to see a large increase of the $\eta_{\text{in-plane}}$ in 160ppm doped sample, a fact that correlates with the anomalous lattice parameter data shown in Figure 8(a). Overall, in general, the lattice perfection of all the crystals was found to be at the same level and very high. An exception to this was found for the 160ppm doped crystal, which showed a broad width in ϕ-direction (Figure 9(d)) that produced a large rise in its $\eta_{\text{in-plane}}$. The exact origin of this is not clear but this might be related to impurity occupying a disordered interstitial lattice site in a manner analogous to the previous studies in Mn^{3+} doped KDP crystals.[25]

Such a model is supported by the measured segregation coefficient for $S_2O_6^{2-}$ presented in Figure 8(c). It shows that at around 160ppm there is a peak value in the segregation coefficient followed by a quick decrease as a function of increased doping concentration. The peak value might be associated with an increase in the defect density increase for the crystal doped at 160ppm, hence lowering its lattice perfection.

3.4 Impurity incorporation model and the mechanism for crystal habit modification

According to the incorporation mechanism proposed by Ristic et al.[5, 6] the $S_2O_6^{2-}$ ions can be incorporated on the $\{\bar{1}\bar{1}\bar{1}\}$ minor tetrahedral faces by the substitution of one of the host ClO_3^- groups of the dithionate ion with the other SO_3 group being expected to protrude out of the crystal surface. In this model, the geometrical and charge similarities between ClO_3^- and $S_2O_6^{2-}$ are important factors to appreciate whilst considering the incorporation of the dithionate ion via substitutional mechanism. Figure 10 shows the respective structures of the two ions after Abrahams & Bernstein[3] ($NaClO_3$) and Kirfel et al.[14] ($Na_2S_2O_6$). The trigonal pyramidal chlorate ion exhibits the distance between the chlorine and oxygen atoms of 1.485 Å with the angle relative to its symmetry axis and the C-O bond being 111.9º (Figure 10(a) and (d)). The $S_2O_6^{2-}$ constitutes two identical trigonal pyramids in a staggered conformation, i.e. twisted by 60º along its S-S bond axis. Each SO_3^- group shows the distance as 1.451 Å between S and O atoms, with an angle of 105.8º relative to S-S and S-O bonds (Figures 10(b) and (e). Figures 10(c) and (f) show a "ClO_3^- shadow" that overlays the Cl and S atoms of the two ions revealing a strong resemblance between the ClO_3^- and SO_3^- groups. Therefore, due to the similarity between the structural configurations of ClO_3^- and SO_3^-, one of SO_3^- group in the $S_2O_6^{2-}$ can occupy a position for ClO_3^- in $NaClO_3$ crystal lattice at the growing surface without much obstruction.

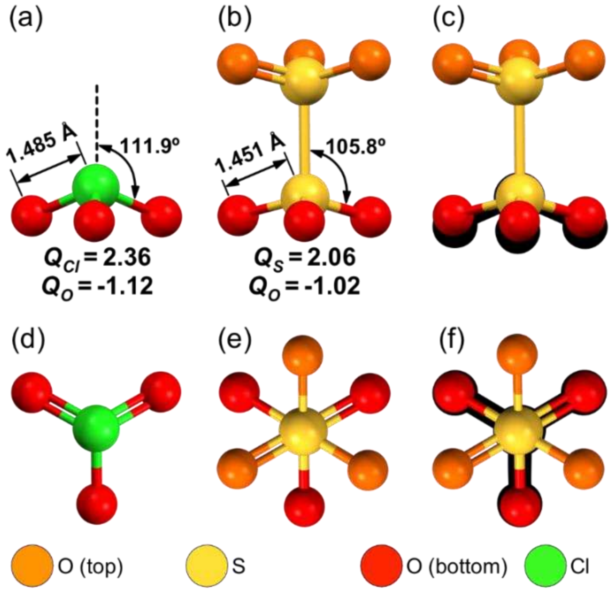

Figure 10. The structures geometry of **(a)** ClO_3^- and **(b)** $S_2O_6^{2-}$ ions. The calculated atomic charge for Cl, O and S atoms are also shown for each molecule. **(c)** A superposition of the $S_2O_6^{2-}$ ion on top of a ClO_3^- "shadow", indicating the close similarity of pyramidal base of these two ions. **(d)**, **(e)** and **(f)** shows a top view of the same representation. Note that the $S_2O_6^{2-}$ O atoms are colored in distinct way to elucidate the opposite configuration of each pyramidal SO_3 group.

Figure 10(a) and (b) shows the results of theoretical calculations for the charges (Q) on atoms of SO_3^- and $S_2O_6^{2-}$ using the semi-empirical PM6 method in the MOPAC2009 code.[26] The Cl and O atoms of the ClO_3^- ion were found to have the elementary charges of 2.36 and -1.12 q, respectively, whilst the S and O atoms for each SO_3^- group from the dithionate ion were found to have values of 2.06 and -1,02, respectively. With this result, it can be seen that the ClO_3^- and the SO_3^- groups at either end of $S_2O_6^{2-}$ have a similar charge distribution. The similarity of charge on the O atoms of ClO_3^- and $S_2O_6^{2-}$ is considered more important than that on the Cl and S atoms because they are shielded by O in the substitution process. The charges on the O of the ClO_3^- and the SO_3^- have a small difference of approximate 10%, which would enable the $S_2O_6^{2-}$ to incorporate in $NaClO_3$ crystal.

Based on the results of the EXAFS analysis (section 3.2), the structural model of the top two growth layers of the $NaClO_3$ $\{\bar{1}\bar{1}\bar{1}\}$ face is shown in Figures 11(a) and (b) which show projected views (top and side views) of the $S_2O_6^{2-}$ incorporation via $\{\bar{1}\bar{1}\bar{1}\}$ surface. A detailed examination into a dithionate incorporated in the crystal bulk reveals that the three O atoms of the upper SO_3^- group, which is not the one substituting a ClO_3^- group, has a very short distance (approximately 0.50Å) to the atomic positions for the O atoms for the three symmetry-related ClO_3^- ions involved in the inter-ionic packing within the next depositing layer, see Figures 11(c) and (d).

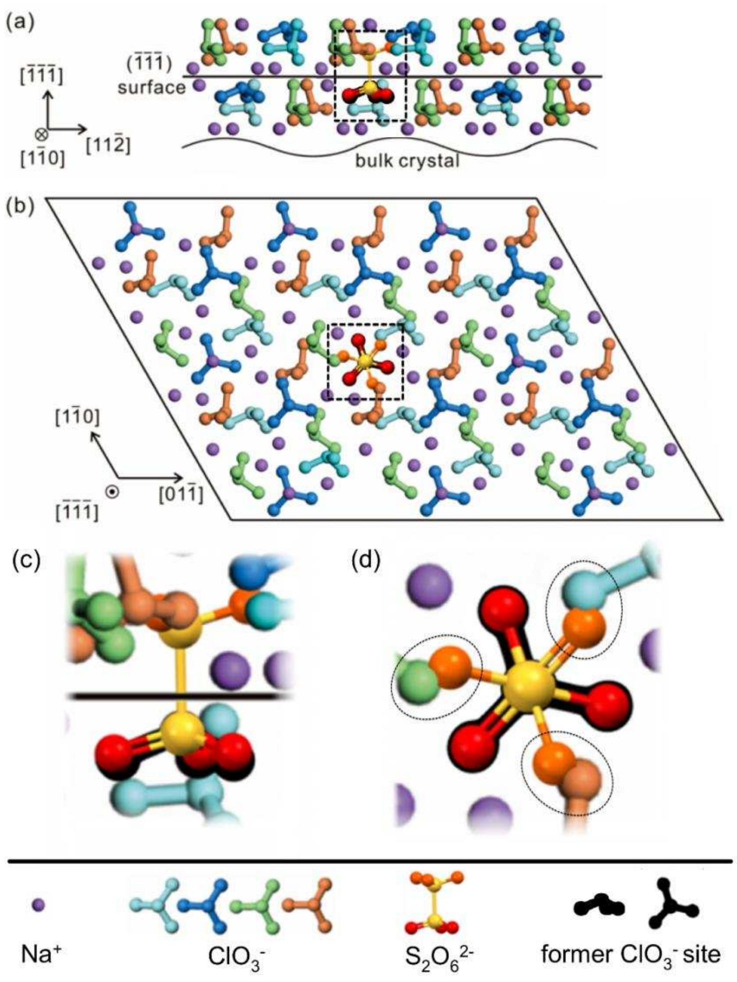

Figure 11. Molecular model of $S_2O_6^{2-}$ in the $NaClO_3$ crystal bulk through the faces of $\{\bar{1}\bar{1}\bar{1}\}$ type based EXAFS results, with an additional depositing molecular layer of $NaClO_3$ on the top of the incorporated $S_2O_6^{2-}$. **(a)** Projection along [1$\bar{1}$0]. The location of the $S_2O_6^{2-}$ is highlighted by the dotted rectangle, and the ClO_3^- groups with four distinct orientations are indicated in four colors.

(b) Projection along $[\bar{1}\bar{1}\bar{1}]$. A closer look in **(c)** and **(d)** shows that upon one SO_3^- of the $S_2O_6^{2-}$ has substituted a ClO_3^-, the O atoms of the other SO_3^- group are expected to displace the O atoms of three different ClO_3^- ions of the next depositing layer due to the incorporation effecting an inter-ionic distance (approximately 0.50Å), highlighted in **(d)**.

As a result, the next depositing ClO_3^- ions would be likely to be repelled by the SO_3^- due to its negative charges of the O atoms, which would result in its expected position being disrupted in terms of being vacated.

As the overall charge of the incorporated $S_2O_6^{2-}$ ion is different from that for the substituted ClO_3^-, to maintain charge balance of the whole crystal after the incorporation of $S_2O_6^{2-}$ at one ClO_3^- site, there are three potential mechanisms structurally disrupting the ClO_3^- deposition in the next growth layer, as presented in Table 5.

Table 5. Potential incorporation mechanisms and the incorporation impact (via substitution and/or vacancy) after $S_2O_6^{2-}$ incorporation to provide a neutral net charge to the crystal.

	Charge change by $S_2O_6^{2-}$ incorporation	**Process**	**Charge change by removing ClO_3^- anions**	**Charge change by removing Na^+ cations**	**Resulted lattice charge**	**Total net charge**
Case 1	-2	One of the three ClO_3^- is removed creating an atomic vacancy.	**ClO_3^-** (substitution) + **ClO_3^-** (vacancy)	-	+2	0
Case 2	-2	Two of the three depositing ClO_3^- could be removed, together with one vicinal Na^+ ions.	**ClO_3^-** (substitution) + **$2(ClO_3^-)$** (vacancy)	**Na^+** (vacancy)	+2	0
Case 3	-2	All the three depositing ClO_3^- could be removed, together with two associated Na^+ ions.	**ClO_3^-** (substitution) + **$3(ClO_3^-)$** (vacancy)	**$2Na^+$** (vacancy)	+2	0

The first (Case 1) of these potential mechanisms would represent the least lattice disruption and hence being the most favorable, when the impurity concentration is low. When one of the depositing ClO_3 ions is vacated, the SO_3 group would tilt to the vacated position and also slightly shift the remaining two ClO_3 ions away from their original positions due to the repulsion between these negatively charged species. There are three potential directions of the S-S bond tilt depending on which ClO_3 ion is removed. A comparison between the ion's dimensions would indicate that the upper SO_3 group is slightly below the vacated ClO_3 position in the $\{\bar{1}\bar{1}\bar{1}\}$ growth direction (e.g. see Figure 11(c)). This would provide some space for the lattice of the incoming grown crystal layers to expand in $\{\bar{1}\bar{1}\bar{1}\}$ direction. The higher the impurity concentration, the more the lattice would be expected to expand. On the other hand, the shift of the two remaining ClO_3 ions approximately in the $\{\bar{1}\bar{1}\bar{1}\}$ plane by the repulsion would further push the neighboring lattice to compress and, again, the higher the impurity concentration, the more the lattice would be expected to compress. This analysis is consistent with the results of XRMD (Section 3.3), i.e. the lattice parameter in $\{\bar{1}\bar{1}\bar{1}\}$ form increases with the impurity concentration, while the lattice parameter in {111} form decreases with the impurity concentration.

The disruption to the crystal lattice also increases with the impurity doping concentration and then the second mechanism (Case 2) can become dominant, i.e. two of three depositing ClO_3 ions are vacated. There are three potential directions of the S-S bond tilt depending on which ClO_3 ion remains. Similarly to the first mechanism, the lattice parameter in $\{\bar{1}\bar{1}\bar{1}\}$ form increases with the impurity concentration, while the lattice parameter in {111} form decreases with the impurity concentration.

The $\{\bar{1}\bar{1}\bar{1}\}$ surfaces of the all the doped crystals with different impurity concentrations appear to be quite smooth, interestingly except for the 160 ppm doped crystal where a number of convex islands across each $\{\bar{1}\bar{1}\bar{1}\}$ surfaces were observed (Figure 12). These islands are consistent with the generation of lattice strain on different growth surface domains that grew with different S_2O_6 impurity incorporation mechanisms, i.e. the first and the second mechanisms, and each of these two mechanisms has three potential directions of tensile strain. When the impurity concentration is low, its incorporation replaces two ClO_3 ions from the crystal (one ClO_3 substituted and one ClO_3 vacated, i.e. the first mechanism). When the impurity concentration is higher than 160ppm, the S_2O_6 incorporation replaces three ClO_3 ions (one ClO_3 inion substituted and two ClO_3 inions with one Na cation vacated, i.e. the second mechanism). However, when the impurity concentration is around 160ppm, S_2O_6 is incorporated with a mixed mechanism of Case 1 and Case 2. The decrease of segregation coefficient when impurity concentration is higher than 160ppm (Figure 8(C)) also indicates the 2nd mechanism is less favorable at low concentration.

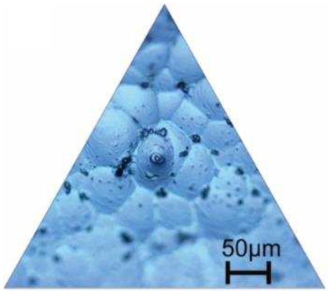

Figure 12. Surface morphology image of the $(\bar{1}\bar{1}\bar{1})$ faces of 160 ppm doped crystal.

If the impurity would be capable to remove two Na cations and three ClO_3 ions in addition to the substituted ClO_3, following the mechanism Case 3 in Table 5, the necessary concentration of $S_2O_6^{2-}$ to achieve such a disturbance to the growing layers would be at least an order of magnitude higher than the ones presented in this work. However, this is a critical mechanism that can completely change orientation of the ClO_3 upcoming growth layer to form the twined crystals. Under such scenario, the upcoming ClO_3 ions have a higher probability to follow the SO_3 orientation in the opposite direction and so disrupt the ClO_3 sequence from this twin originating point. This mechanism of vacating three ClO_3 ions is consistent with the structural model reported in the previous work.[7]

4 Conclusion

Pure sodium chlorate single crystals bounded by $\{100\}$ and $\{110\}$ forms were grown from aqueous solution, as well as the $S_2O_6^{2-}$-doped crystals bounded by minor tetrahedral $\{\bar{1}\bar{1}\bar{1}\}$ forms. A potential mechanism of this $S_2O_6^{2-}$ incorporation draws upon the results obtained from several techniques. The XRF map revealed the non-equivalent $S_2O_6^{2-}$ concentration in the {001} and $\{\bar{1}\bar{1}\bar{1}\}$ growth sector, with the latter being preferred over the former one. It clearly shows a high selectivity by the dithionate ion regarding the attachment surface during the crystal growth. Local structural probing made by polarized EXAFS at the S K-edge in two orthogonal directions indicates that the S-S bond orientation is mainly aligned with the $[\bar{1}\bar{1}\bar{1}]$. Calculation of the atomic charge distributions between ClO_3^{1-} and $S_2O_6^{2-}$ supports the substitution mechanism of ClO_3^{1-} by $S_2O_6^{2-}$. Incorporation modeling was made considering the S-S bond direction along the $[\bar{1}\bar{1}\bar{1}]$ is consistent with one terminal SO_3 group on the dithionate ions substituting for chlorate ions in the host crystal and the other SO_3 group in the ion disturbing the inter-ionic packing for the succeeding growth layers. Examination of the incorporated site chemistry shows that the protruding SO_3 group leaves no space for the O atoms for the adsorption of the further ClO_3 ions in the subsequent growth layer which are, in turn, repulsed by the dithionate crystal surface and leaves its site vacated. This is supported by the charge balance approach that represents the least lattice disruption scenario for the impurity incorporation and so suggests a slightly 3-fold symmetry tilt of the S-S bond towards the vacant ClO_3 ion sites in respect to the $[\bar{1}\bar{1}\bar{1}]$ direction. High resolution X-ray diffraction studies using XRMD reveal suppression of $(3\bar{4}3)(3\bar{4}1)$ and (343)(341) four-beam (002) RS secondary peaks in crystals prepared in the presence of the dithionate impurity. Structure factors calculations were found to be consistent with the displacement of oxygen atoms. Analysis of the lattice parameters revealed a slight trigonal distortion along the <111> ($\Delta d/d \sim 4.6 \times 10^{-4}$). The (002) RS detected a tensile strain and a compressive strain in the impurity doped crystal sectors by applying the secondary reflections of $(1\bar{1}1)$/$(\bar{1}11)$ and (111)/$(\bar{1}\bar{1}1)$ respectively. These strains caused the lattice parameter change in the opposite variation trends in the two different regions of the crystal, which supports the mechanisms of the impurity incorporation proposed in this work. The strain was concluded to have contributed to the formation of $\{\bar{1}\bar{1}\bar{1}\}$ type faces in terms of reducing their growth rate. The overall quality of most crystals was not found to change significantly, except that the 160 ppm crystal, which was of much lower crystal perfection. This was attributed to the different lattice parameters of the local crystal domains with the different growth mechanisms associated the absence of one and two ClO_3^- ions following the impurity incorporation.

Whilst the EXAFS investigation provided information about the impurity structure with respect to the crystal and hence the mechanisms of the crystal habit modification, XRMD provided the strong experimental evidence supporting the mechanism proposed in the study.

Acknowledgments

The authors gratefully acknowledge Professor Helmut Klapper from the Institute of Crystallography at RWTH Aachen, Germany, for useful discussions and for providing the X-ray topograph shown in Figure 2. This work forms a part of the doctoral degree studies (Z.L.).[27] G.A.C. thankfully acknowledges the support of CNPq, Brazil (Programa Ciência sem Fronteiras – SWE 234550/2014-7) for the support of a visiting scholarship to the EPSRC Centre for Doctoral Training in Complex Particulate Products and Processes at the University of Leeds, UK. Two of us (X.L. and K.J.R.) gratefully acknowledge the UK's EPSRC for their support in crystallization research at the Universities of Leeds and Manchester through their funding of the Critical Mass Project "Molecules, Clusters and Crystals" (Grant References EP/I014446/1 and EP/I013563/1, respectively). We also acknowledge the CNPq, FAPEMA, FAEPEX-UNICAMP (Brazil) for their financial support. Synchrotron beam time for the EXAFS and XRMD experiments was provided by the Diamond Light Source and the LNLS which we gratefully acknowledge.

References

(1) Clydesdale, G.; Roberts, K. J.; Docherty, R., Modeling the Morphology of Molecular-Crystals in the Presence of Disruptive Tailor-Made Additives. J. Cryst. Growth **1994,** 135, (1-2), 331-340.
(2) Clydesdale, G.; Roberts, K. J.; Lewtas, K.; Docherty, R., Modeling the Morphology of Molecular-Crystals in the Presence of Blocking Tailor-Made Additives. J. Cryst. Growth **1994,** 141, (3-4), 443-450.
(3) Abrahams, S. C.; Bernstein, J. L., Remeasurement of Optically-Active $NaClO_3$ and $NaBrO_3$. Acta Crystallogr., Sect. B: Struct. Sci **1977,** 33, 3601-3604.
(4) Buckley, H. E., The influence of RO4 and related ions on the crystalline form of sodium chlorate. Z. Kristallogr. **1930,** 75, (1-2), 15-31.
(5) Ristic, R.; Sherwood, J. N.; Wojciechowski, K., Morphology and Growth-Kinetics of Large Sodium-Chlorate Crystals Grown in the Presence and Absence of Sodium Dithionate Impurity. J. Phys. Chem. **1993,** 97, (41), 10774-10782.
(6) Ristic, R.; Shekunov, B. Y.; Sherwood, J. N., Growth of the Tetrahedral Faces of Sodium-Chlorate Crystals in the Presence of Dithionate Impurity. J. Cryst. Growth **1994,** 139, (3-4), 336-343.
(7) Lan, Z.-P.; Lai, X.; Roberts, K.; Klapper, H., X-ray Topographic and Polarized Optical Microscopy Studies of Inversion Twinning in Sodium Chlorate Single Crystals Grown in the Presence of Sodium Dithionate Impurities. Cryst. Growth & Des. **2014,** 14, (11), 6084-6092.
(8) Clydesdale, G.; Roberts, K. J.; Telfer, G. B.; Saunders, V. R.; Pugh, D.; Jackson, R. A.; Meenan, P., Prediction of the Polar Morphology of Sodium Chlorate Using a Surface-Specific Attachment Energy Model. J. Phys. Chem. B **1998,** 102, (36), 7044-7049.
(9) Catti, M.; Ferraris, G., Twinning by Merohedry and X-Ray Crystal-Structure Determination. Acta Crystallogr., Sect. A **1976,** 32, 163-165.
(10) Hahn, T.; Kappler, H., Twinning of crystals. Int. Tables Crystallogr. Vol. D, Kluwer Academic: Dordrecht, 2003; pp 393-448.
(11) Koningsberger, D. C.; Prins, R., X-ray absorption: principles, applications, techniques of EXAFS, SEXAFS, and XANES. Wiley: New York, 1988.
(12) Chang, S. L., X-Rays Multiple-Wave Diffraction: Theory and Application. Springer Verlag: New York, 2004; Vol. 143.
(13) Ravel, B.; Newville, M., ATHENA, ARTEMIS, HEPHAESTUS: data analysis for X-ray absorption spectroscopy using IFEFFIT. J. Synchrotron Radiation **2005,** 12, (4), 537-541.
(14) Kirfel, A.; Will, G.; Weiss, A., X-Ray-Diffraction Study of $Na_2S_2O_6.2H_2O$ and $Na_2S_2O_6.2D_2O$. Acta Crystallogr., Sect. B: Struct. Sci **1980,** 36, (Feb), 223-228.
(15) Sole, V. A.; Papillon, E.; Cotte, M.; Walter, P.; Susini, J., A multiplatform code for the analysis of energy-dispersive X-ray fluorescence spectra. Spectrochim. Acta, Part B **2007,** 62, (1), 63-68.
(16) Cusatis, C.; Kobayashi Franco, M.; Kakuno, E.; Giles, C.; Morelhao, S.; Mello, V., Jr; Mazzaro, I., A versatile X-ray diffraction station at LNLS (Brazil). J. Synchrotron Radiation **1998,** 5, (3), 491-493.

(17) Rossmanith, E., UMWEG: a program for the calculation and graphical representation of multiple-diffraction patterns. J. Appl. Crystallogr. **2003,** 36, (6), 1467-1474.

(18) Butterworth Lab. http://butterworth-labs.co.uk/

(19) Morelhão, S. L.; Cardoso, L. P., X-ray Multiple Diffraction Phenomenon in the Evaluation of Semiconductor Crystalline Perfection. J. Appl. Crystallogr. **1996,** 29, (4), 446-456.

(20) Remédios, C. M. R.; Paraguassu, W.; Lima, J. A.; Freire, P. T. C.; Mendes, J.; Melo, F. E. A.; de Menezes, A. S.; dos Santos, A. O.; Cardoso, L. P.; Miranda, M. A. R., Effect of Ni(II) doping on the structure of L-histidine hydrochloride monohydrate crystals. J. Phys.: Condens. Matter **2008,** 20, (27), 275209.

(21) Morelhao, S. L.; Remedios, C. M. R.; Freitas, R. O.; dos Santos, A. O., X-ray phase measurements as a probe of small structural changes in doped nonlinear optical crystals. J. Appl. Crystallogr. **2011,** 44, 93-101.

(22) Morelhão, S. L.; Cardoso, L. P., Structural properties of heteroepitaxial systems using hybrid multiple diffraction in Renninger scans. J. Appl. Phys. **1993,** 73, (9), 4218-4226.

(23) Ristic, R. I.; Sherwood, J. N.; Shripathi, T., The influence of tensile strain on the growth of crystals of potash alum and sodium nitrate. J. Cryst. Growth **1997,** 179, (1-2), 194-204.

(24) Ristic, R. I.; Shekunov, B. Y.; Sherwood, J. N., The influence of synchrotron radiation-induced strain on the growth and dissolution of brittle and ductile materials. J. Cryst Growth **1997,** 179, (1-2), 205-212.

(25) Remédios, C. M. R.; dos Santos, A. O.; Lai, X.; Roberts, K. J.; Moreira, S. G. C.; Miranda, M. A. R.; de Menezes, A. S.; Rouxinol, F. P.; Cardoso, L. P., Experimental Evidence for the Influence of Mn^{3+} Concentration on the Impurity Incorporation and Habit Modification Mechanism of Potassium Dihydrogen Phosphate. Cryst.l Growth & Des. **2010,** 10, (3), 1053-1058.

(26) Stewart, J. J. P., Optimization of parameters for semiempirical methods V: Modification of NDDO approximations and application to 70 elements. J. Mol. Model. **2007,** 13, (12), 1173-1213.

(27) Lan, Z.-P. The Structural Role of Sodium Dithionate Impurity in the Habit Modification of Sodium Chlorate Single Crystals. PhD thesis, University of Leeds, 2013.

supporting information is available:

1. SUPPLEMENTARY MATERIAL

For Table of Contents Use Only

Characterization of the Structural Environment of Dithionate Ions Associated with their Role in the Crystal Habit Modification of Sodium Chlorate

Zhipeng Lan, Guilherme A. Calligaris, Alan S. de Menezes,
Adenilson O. dos Santos, Xiaojun Lai, Lisandro P. Cardoso and Kevin J. Roberts

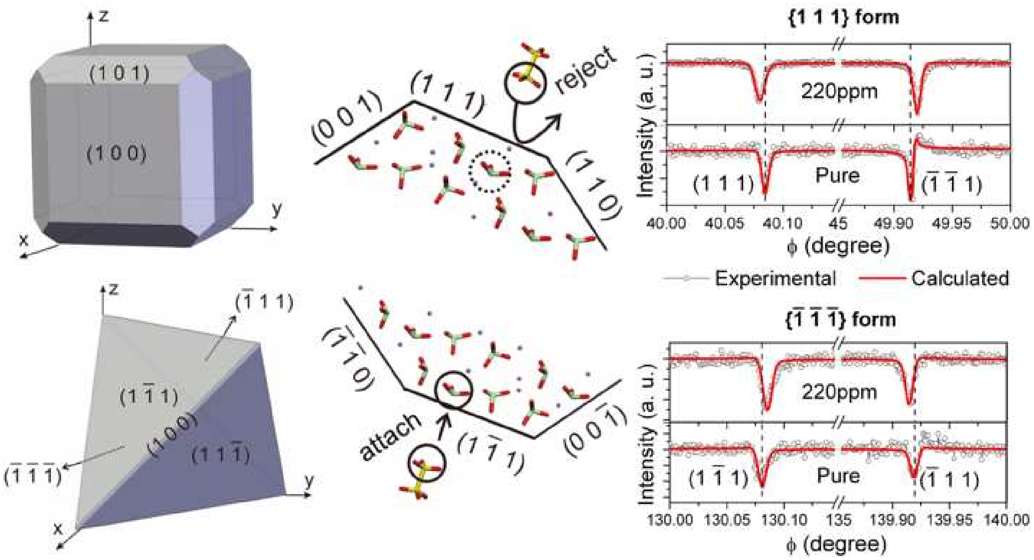

Synopsis: $NaClO_3$ crystal morphology changes from a cuboid to a tetrahedron of $\{\bar{1}\bar{1}\bar{1}\}$ when grown in presence of Na_2SO_6 impurity. EXAFS and X-ray Multiple Diffraction reveal that one SO_3 substitutes a host ClO_3 at the $\{\bar{1}\bar{1}\bar{1}\}$ growth interface and creates one or more lattice vacancies of ClO_3, of which the three vacancies is the case forming twinning crystals.